ORIGINAL ARTICLE

A modular multilevel converter with active power filter (APF-MMC) under low-frequency operation

Guanlong Jia[1] · Mingshuo Li[1] · Lin Chen[1] · Binhao Shi[1] · Feng Niu[1] · Yu Tang[1]

Abstract

In the realm of medium/high voltage applications, the modular multilevel converter with an active power filter (APF-MMC) emerges as a technology that eliminated the inherent voltage fluctuations of larger sub-module (SM) capacitors. However, the introduced APF circuit in each phase can only deal with power in even frequencies, and the APF-MMC cannot be directly applied in the field of motor drives with low-frequency operation. In this paper, based on the APF-MMC topology, by adding two high-frequency variables as control degrees of freedom, the base frequency power is transferred to high-frequency power, which can considerably minimize the capacitor voltage ripple in the low-frequency region of the topology. In addition, the influence of the injected high-frequency variables on the output characteristics of the topology is eliminated by controlling the APF circuit as hardware degree of freedom. Its equivalent circuit and operating principle are introduced in detail. Concurrently, a control method is proposed for the APF circuit, ensuring seamless operation of the converter. Finally, through a combination of simulation and experimental results, it is demonstrated that the APF-MMC topology surpasses the conventional MMC in its efficacy under low-frequency operation.

Keywords Modular multilevel converter · Capacitor voltage ripple · Degrees of freedom · Low frequency

1 Introduction

The modular multilevel converter (MMC) has been extensively researched in HVDC transmission system and motor drives [1–3] because of its efficiency, highly modularity and extensibility, and superior output signal quality [4]. When compared with conventional converters like flying capacitor and cascaded H-bridge (CHB) converters, the utilization of the MMC topology enables the preservation of substantial reactive components in medium/high voltage high power ranges, including line transformers, harmonic filters, and dc bus capacitors [5].

The extensive use of sub-module (SM) capacitors causes heavier weight and higher cost, which hinders the further application of MMC. What is worse, the voltage fluctuation of the SM is in a reverse ratio with the operating frequency. Thus, a large capacitor is required to restrain the voltage ripple when operating at low frequencies. It is evident from

actual engineering application that SM capacitors occupy approximately half of the system volume and most of the system weight [6]. Hence, capacitor voltage ripple must be reduced, resulting in a smaller capacitance [7].

Since the MMC topology was first proposed in [8], a great deal of research has been done on diminishing SM voltage fluctuation, and this research is mainly divided into two kinds of methods, adding control variable degrees of freedom and adding hardware degrees of freedom [9–18]. In terms of adding control variable degrees of freedom, in [9] and [10], a second-order circuiting current was infused to arms of each phase to suppress the voltage ripple in the SM. Methods for injecting second-order and fourth-order circuiting currents into arm currents were proposed in [11] and [12]. The aforementioned methods are effectual when the voltage modulation index is high [13]. However, they are not applicable for motor drive systems that require wide range adjustment [11]. Moreover, the above methods only handle even-order frequency powers. However, these are not the critical portions that cause voltage fluctuation [12]. A mixed injection strategy of high-frequency sinusoidal current with voltage was initially put forth in [14] to handle the base frequency power in SM capacitors. Capacitor voltage

✉ Lin Chen
  764098881@qq.com

[1] State Key Lab of Reliability and Intelligence of Electrical Equipment, Hebei University of Technology, Tianjin, China

fluctuation can be effectively decreased using this method. However, the current stress and power dissipation on the switch devices are significantly increased, particularly when the voltage modulation index is low [6]. To diminish the maximum of arm current, other high-frequency component waveforms are introduced, such as square wave [15–17]. However, a related high-frequency voltage emerges in the arm voltage reference value, that could result in overmodulation [6, 18]. In addition, the infused voltage produces electromagnetic interference and even causes motor insulation breakdown [19].

To avert the above drawbacks of adding control variable degrees of freedom, the suppression of SM voltage fluctuation is achieved by adding hardware degrees of freedom to the MMC [20–26]. In [20, 21], a novel active power filtering decoupling circuit was proposed, which utilizes inductors and capacitors as energy storage devices and adds a power switching arm. Through the precise control of the additional arm and the MMC main circuit, the ripple suppression of the SM capacitor was successfully achieved. It is worth noting that these methods involve coupling effects between the active power filter circuit and the MMC main topology, leading to additional switching actions and ultimately increasing the total power loss of the system. Meanwhile, the authors of [22–25] proposed an independent decoupling circuit for active power filters, which uses inductors or capacitors as energy storage components and is connected in parallel at both ends of the dc bus capacitor. However, due to the relatively low energy storage density of inductors, additional active power filter decoupling circuits often occupy a larger volume, reducing the power density of the system. In [26], it was proposed that an active power filter (APF) circuit be inserted to the per phase of the MMC, which is called APF-MMC. This topology addresses only the even-order frequency powers in SMs.

In this paper, an extension of the APF-MMC introduced in [26] is presented. The basic principle is to manage the two control degrees of freedom of the injected high-frequency component to achieve SM voltage ripple suppression, and to use the hardware degree of freedom of the additional APF circuit to mitigate the impact of the injected high-frequency voltage with the external characteristics. The frequency of the control degrees of freedom in the APF-MMC can be controlled, which means they can better adapt to operation in a wide frequency range and avoid overmodulation.

2 Proposed APF-MMC topology

2.1 Basic configuration of the APF-MMC

Figure 1a presents the APF-MMC topology, which is made up of phases x ($x = a, b, c$). Every phase includes two duplicate arms, called the upper arm and the lower arm, and one parallel-connected Buck-type APF branch. Every arm is equipped with an inductor L and $2N$ half-bridge SMs. Furthermore, each of the arms can be further divided into a top sub-arm and a bottom sub-arm, each consisting of N SMs. The lower-half arm located in the upper arm and the upper-half arm situated in the lower arm are called middle arms (Mid-arms), as depicted in Fig. 1a. Both the APF circuit and the SM can be substituted with various topology structures [27]. In addition, the Mid-SM does not exert any substantial influence on the ac output side.

It is assumed that the output voltage e_x and the output current i_x of the APF-MMC circuit are

$$\begin{cases} e_x = E_x \sin(\omega t + \theta_x) \\ i_x = I_x \sin(\omega t + \theta_x - \varphi) \end{cases}, \tag{1}$$

Fig. 1 APF-MMC topology: **a** configuration; **b** equivalent model
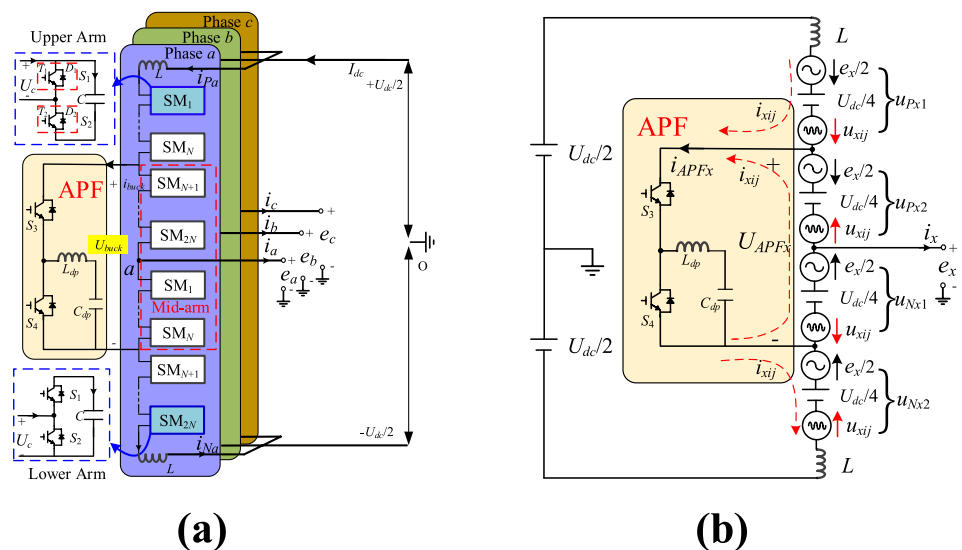
where E_x and I_x (subscript $x = a, b, c$) are the peak output voltage and the peak current, respectively. ω is the output angular frequency of the fundamental, and θ_x and φ are the phase angle and the power factor angle, respectively.

By disregarding the voltage drop across the arm inductor [28], the arm voltages u_{Px} and u_{Nx} of the APF-MMC are described as

$$\begin{cases} u_{Px} = \dfrac{1}{2}U_{dc} - e_x = \dfrac{1}{2}U_{dc} - E_x\sin(\omega t + \theta_x) \\ u_{Nx} = \dfrac{1}{2}U_{dc} + e_x = \dfrac{1}{2}U_{dc} + E_x\sin(\omega t + \theta_x). \end{cases} \quad (2)$$

Similarly, the corresponding arm currents i_{Px} and i_{Nx} are

$$\begin{cases} i_{Px} = \dfrac{1}{3}I_{dc}[1 + m\sin(\omega t + \theta_x - \varphi)] + I_{2f}\cos(2\omega t + 2\theta_x - \varphi) \\ i_{Nx} = \dfrac{1}{3}I_{dc}[1 - m\sin(\omega t + \theta_x - \varphi)] + I_{2f}\cos(2\omega t + 2\theta_x - \varphi). \end{cases} \quad (3)$$

2.2 Operating principle of the APF-MMC

For convenient understanding of the operating principle, the equivalence structure of the APF-MMC is exhibited in Fig. 1b. In the model, controlled voltage sources are used to substitute for the sub-arms, and the desirable sub-arm output voltages u_{Px1}, u_{Px2}, u_{Nx1}, and u_{Nx2} in each phase are postulated to be composed of three dominant elements of dc voltage components ($U_{dc}/4$), fundamental frequency ac voltage ($e_x/2$), and high-frequency ac voltage u_{xij}. To keep the dc voltage consistent, the dc components of the sub-arm in each phase are set to identical directions, while the ac voltages of the arm are arranged in contrary directions to generate differential voltage to be sent to the output.

As signified in Fig. 1b, the sign of the injected high-frequency voltage of the top and bottom arms is inverted in each arm to prevent the high-frequency voltage from affecting the topology output side. The sub-arm voltage can be realized by controlling the modulation wave of the corresponding sub-arm [6]. In addition, the expressions of sub-arm voltages are

$$\begin{cases} u_{Px1} = \dfrac{U_{dc}}{4} - \dfrac{e_x}{2} - u_{xij} \\ u_{Px2} = \dfrac{U_{dc}}{4} - \dfrac{e_x}{2} + u_{xij} \\ u_{Nx1} = \dfrac{U_{dc}}{4} + \dfrac{e_x}{2} - u_{xij} \\ u_{Nx2} = \dfrac{U_{dc}}{4} + \dfrac{e_x}{2} + u_{xij}. \end{cases} \quad (4)$$

There are three degrees of freedom in the APF-MMC circuit, which are the high-frequency voltage u_{xij}, the high-frequency ac current i_{xij}, and the APF circuit branch, to reconstruct the fluctuation power of the sub-arm and to eliminate the effect of high-frequency voltage on the ac output voltage. Similar to the methods in [14] and [15], the high-frequency components u_{xij} and i_{xij} are used as two degrees of freedom to convert low-frequency fluctuation powers into high-frequency ripple powers to diminish the capacitor voltage fluctuation. In addition, the APF circuit is taken as a hardware degree of freedom, supplies a route for the current i_{xij} in the Mid-SMs and eliminates the effects of the injected voltage u_{xij} on the external features of the MMC.

Due to the presence of the arm inductor L, the high-frequency current i_{xij} of the top sub-arm and the bottom sub-sum can be generated by controlling the voltage on the relevant arm inductor L [4]:

$$i_{xij} = \frac{1}{L}\int u_{Lxij}\,\mathrm{d}t, \quad (5)$$

where u_{Lxij} is the drop voltage on the arm inductor L. In addition, the currents of the top sub-arm in the upper arm and the bottom sub-sum in the lower arm i_{Px1} and i_{Nx2} can be derived as

$$\begin{cases} i_{Px1} = \dfrac{I_{dcir}}{3} + \dfrac{i_x}{2} + i_{xij} \\ i_{Nx2} = \dfrac{I_{dcir}}{3} - \dfrac{i_x}{2} + i_{xij} \end{cases}, \quad (6)$$

where I_{dcir} is the circuiting current, which is calculated as

$$I_{dcir} = I_{dc} + 3i_{cir}. \quad (7)$$

The second-order circuiting current i_{cir} can be effectively eliminated through the utilization of a circuiting current suppression controller (CCSC) [29]. Assuming that there is no second-order component in the circuiting current, I_{dcir} can be rewritten as

$$I_{dcir} = I_{dc}. \quad (8)$$

The high-frequency current i_{xij} of the Mid-SMs can be generated by controlling the APF circuit current i_{APFx}.

$$i_{APFx} = 2i_{xij}. \quad (9)$$

On the basis of Kirchhoff's current law, the arms currents i_{Px2} and i_{Nx1} are derived as

$$\begin{cases} i_{Px2} = \dfrac{I_{dc}}{3} + \dfrac{i_x}{2} - i_{xij} \\ i_{Nx1} = \dfrac{I_{dc}}{3} - \dfrac{i_x}{2} - i_{xij}. \end{cases} \quad (10)$$

In the APF-MMC, the momentary energies within the sub-arms are acquired through the multiplication of the sub-arm current and voltage. The powers are obtained as

$$\begin{cases} p_{Px1} = u_{Px1}i_{Px1} = p_1 + p_2 + p_3 \\ P_{Px2} = u_{Px2}i_{Px2} = p_1 + p_2 - p_3 \\ p_{Nx1} = u_{Nx1}i_{Nx1} = p_1 - p_2 - p_3 \\ P_{Nx2} = u_{Nx2}i_{Nx2} = p_1 - p_2 + p_3, \end{cases} \quad (11)$$

where p_{Px1} and p_{Px2} are the powers of the upper arm. p_{Nx1} and p_{Nx2} are the powers of top and bottom sub-arm in the lower arm, respectively. In addition, p_1, p_2, and p_3 can be expressed as (12):

$$\begin{cases} p_1 = \dfrac{U_{dc}I_{dc}}{12} - \dfrac{E_xI_x}{8}\cos\varphi + \dfrac{E_xI_x}{8}\cos(2\omega t + 2\theta_x - \varphi) \\ p_2 = \dfrac{U_{dc}I_x}{8}\sin(\omega t + \theta_x - \varphi) - \dfrac{E_xI_{dc}}{6}\sin(\omega t + \theta_x) - u_{xij}i_{xij} \\ p_3 = \dfrac{U_{dc}i_{xij}}{4} - \dfrac{u_{xij}I_{dc}}{3} - \dfrac{E_xi_{xij}}{2}\sin(\omega t + \theta_x) - \dfrac{u_{xij}I_x}{2}\sin(\omega t + \theta_x - \varphi). \end{cases} \quad (12)$$

In (12), the initial two components of p_1 correspond to the direct current (dc) powers of the system. It is imperative for these values to be zero to maintain system stability [30], and the third term of p_1 is the second-order fluctuation power. In addition, the first two terms of p_2 are the base frequency powers, which are the major causes of the voltage ripple, and the third term of p_2 consists of two controllable variable degrees of freedom. Similarly, each term of p_3 contains a controllable variable degree of freedom. Because each degree of freedom is a high-frequency variable, its impact on the SM capacitor voltage ripple is relatively small and negligible [31].

According to [14] and [29], square waves and other waveforms can be selected as the injected high-frequency components to diminish the arm current amplitude. For the convenience of analysis, a sine waveform is selected as the infused high-frequency voltage, as follows:

$$u_{xij} = U_{xij}\sin(\omega_h t + \theta_h) = U_{xij}\sin(2\pi f_h t + \theta_h), \quad (13)$$

where ω_h is the angular velocity, and θ_h and f_h are the initial phase angle and the output angular frequency. To significantly diminish the capacitor voltage ripple, f_h is generally specified as 4–10 times the working frequency f. At the same time, f_h ought to be no higher than 1/10 of the tantamount switch frequency of the MMC topology to accurately control the high-frequency variables [13].

By controlling the two degrees of freedom of the infused high-frequency voltage and current, the base frequency power in the sub-arms is converted to high-frequency power, realizing the suppression of voltage ripple [14]. Then the high-frequency current is expressed as [31]

$$i_{xij} = \left[\dfrac{E_xI_{dc}}{3}\sin(\omega t + \theta_x) - \dfrac{U_{dc}I_x}{4}\sin(\omega t + \theta_x - \varphi)\right]U_{xij}^{-1}\sin(\omega_h t + \theta_h). \quad (14)$$

Substituting (14) into (12), p_2 can be obtained as

$$p_2 = \left[\dfrac{U_{dc}I_x}{8}\sin(\omega t + \theta_x - \varphi) - \dfrac{E_xI_{dc}}{6}\sin(\omega t + \theta_x)\right]\cos(2\omega_h t + 2\theta_h). \quad (15)$$

As indicated by Eq. (14), the value of i_{xij} is reversed proportional to the maximum value of the high-frequency voltage. To reduce the amplitude of the injected high-frequency current and to prevent overmodulation, [29] suggests calculating the amplitude value of the high-frequency voltage based on the instantaneous magnitude of the output voltage. The amplitude should meet the following mathematical relations:

$$U_{xij} = \dfrac{U_{dc}}{4} - \dfrac{\max(|e_a|, |e_b|, |e_c|)}{2}, \quad (16)$$

where $\max(|e_x|)$ is meant to take the largest value of $|e_x|$.

When the value of the injected high-frequency voltage is gained by (16), although the infused current can be minimized, the calculation of the variable voltage amplitude aggravates the complicacy and affects the robustness and redundancy of the system [13]. For this reason, the most commonly used expression for calculating the infused voltage is

$$U_{xij} = \dfrac{U_{dc}}{4} - \dfrac{E_x}{2}. \quad (17)$$

On the basis of the above discussion, the equations for the injected high-frequency elements are as follows:

$$\begin{cases} u_{xij} = \dfrac{U_{dc} - 2E_x}{4}\sin(\omega_h t + \theta_h) \\ i_{xij} = \dfrac{[4E_xI_{dc}\sin(\omega t + \theta_x) - 3U_{dc}I_x\sin(\omega t + \theta_x - \varphi)]\sin(\omega_h t + \theta_h)}{3U_{dc} - 6E_x}. \end{cases} \quad (18)$$

Substituting (18) into (12), the sub-arm powers can be derived as

$$\begin{cases} p_1 = \dfrac{E_xI_x}{8}\cos(2\omega t + 2\theta_x - \varphi) \\ p_2 = \left[\dfrac{U_{dc}I_x}{8}\sin(\omega t + \theta_x - \varphi) - \dfrac{E_xI_{dc}}{6}\sin(\omega t + \theta_x)\right]\cos(2\omega_h t + 2\theta_h). \\ p_3 = \dfrac{U_{dc}i_{xij}}{4} - \dfrac{u_{xij}I_{dc}}{3} - \dfrac{E_xi_{xij}}{2}\sin(\omega t + \theta_x) - \dfrac{u_{xij}I_x}{2}\sin(\omega t + \theta_x - \varphi) \end{cases} \quad (19)$$

Comparing (12) with (19), the basic frequency fluctuation power in the arm is completely replaced by the high-frequency fluctuation powers. Then the ripple powers in arms are basically constituted of second-order and high-frequency parts. Unlike the classical MMC arm powers, because ω_h is greater than ω, the high-frequency ripple powers in (19) significantly increase the charging and discharge frequency of the arm capacitor, greatly alleviating the variability in the capacitor voltage, and the smaller the angular frequency

ω, the better the capacitor voltage ripple suppression effect [19].

2.3 Operating principle of the APF branch

According to Fig. 1b, the voltage U_{APFx} is equal to $U_{dc}/2$. Subsequently, the power p_{APFx} assimilated by the capacitor C_{dp} in the APF circuit is shown in (20):

$$p_{APFx} = \frac{U_{dc}i_{APFx}}{2}. \tag{20}$$

Substituting (18) into (20), p_{APFx} can be re-calculated as

$$p_{APFx} = \frac{4E_x U_{dc} I_{dc} \sin(\omega t + \theta_x) \sin(\omega_h t + \theta_h)}{3U_{dc} - 6E_x} - \frac{U_{dc}^2 I_x \sin(\omega t + \theta_x - \varphi) \sin(\omega_h t + \theta_h)}{U_{dc} - 2E_x}. \tag{21}$$

Only when the buck-type APF branch is controlled to operate in the boundary conduction mode (BCM) or the discontinuous current mode (DCM) mode [32], the power shown in (21) is completely absorbed by the capacitor C_{dp} in the APF branch so that

$$C_{dp} \frac{dv_{dp}}{dt} v_{dp} = p_{APFx}, \tag{22}$$

where v_{dp} represents the capacitor voltage of C_{dp}. In addition, the integral (22), the APF branch energy W_{APF} is expressed as

$$W_{APF} = \frac{1}{2} C_{dp} v_{dp}^2 = \int p_{APFx} dt = W_{APFx} + W_{APF0}, \tag{23}$$

where W_{APFx} is the fluctuation energy of every phase. W_{APF0}, a constant intricately associated with the energy storage efficiency, governs the direct current deviation of v_{dp} [6].

Combining (21) and (23), the expressions of v_{dp} and i_{dp} are described as (24) and (25), respectively:

frequency f_{APF} is independent of the switching frequency of the SMs.

$$f_{LC} = \frac{1}{2\pi \sqrt{L_{dp} C_{dp}}} = \lambda f_{APF}, (1/10 < \lambda < 1/5). \tag{26}$$
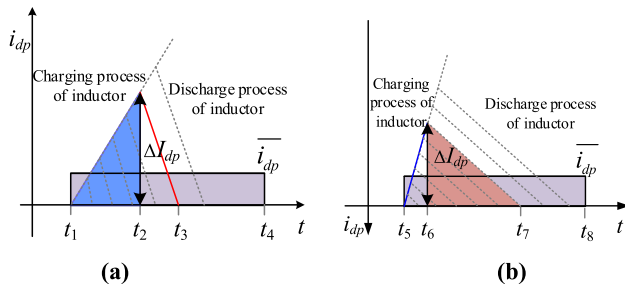
3 Control and analysis of the APF circuit

The primary objective of the APF is the generation of the required high-frequency current i_{xij} in the Mid-arms. Since the switching frequency of the APF circuit is much higher than the operating frequency that needs to be controlled to generate the high-frequency current, the input voltage U_{APF} and the decoupling capacitor voltage v_{dp} in the APF branch can be considered as constants in one switching period T_{APF}. At this time, the decoupling inductor L_{dp} in the APF circuit can be regarded as linear charging or linear discharge in one switching cycle. Thus, the change rate of inductor current can be considered a constant, as shown in Fig. 2.

Figure 2a displays the charging process from the MMC to the inductor L_{dp} and the capacitor C_{dp} of the APF circuit. At $t=t_1$, the power switching device S_3 turns on and S_4 turns off, and the APF circuit works in the Buck state. At this time, the inductor current i_{dp} in the APF circuit increases linearly. Equation (27) indicates the mathematical logic between the capacitor voltage v_{dp} and the current i_{dp} in the APF circuit. In addition, the change rate of the inductor current k_1 is shown in (28). At $t=t_2$, the power switching device S_3 turns off and S_4 turns on. The inductor L_{dp} in the APF circuit begins to release energy to the capacitor C_{dp}, and when $t=t_3$, the energy in the inductor L_{dp} is conveyed to the capacitor C_{dp}. At this time, the voltage v_{dp} and the current i_{dp} of the capacitor have the mathematical relationship shown in (29). T_{APF} is the switching period of the APF circuit, and its calculation is shown in (30):

$$v_{dp} = \sqrt{\frac{2}{C_{dp}}(W_{APFx} + W_{APF0}} = \sqrt{\begin{array}{l} \dfrac{4U_{dc}E_x I_{dc} \sin[(\omega_h - \omega)t + \theta_h - \theta_x]}{3U_{dc} - 6E_x)C_{dp}(\omega_h - \omega)} - \dfrac{U_{dc}^2 I_x \sin[(\omega_h - \omega)t + \theta_h - \theta_x + \varphi]}{U_{dc} - 2E_x)C_{dp}(\omega_h - \omega)} \\ + \dfrac{U_{dc}^2 I_x \sin[(\omega_h + \omega)t + \theta_h + \theta_x - \varphi]}{U_{dc} - 2E_x)C_{dp}(\omega_h + \omega)} - \dfrac{4U_{dc}E_x I_{dc} \sin[(\omega_h + \omega)t + \theta_h + \theta_x]}{3U_{dc} - 6E_x)C_{dp}(\omega_h + \omega)} + \dfrac{2W_{dp0}}{C_{dp}} \end{array}}, \tag{24}$$

$$i_{dp} = \frac{p_{APFx}}{v_{dp}}. \tag{25}$$

In addition, to effectively suppress the switching harmonics, it is crucial to ensure that the resonant frequency f_{LC} of the APF circuit is approximately $1/10 \sim 1/5$ of the switching frequency f_{APF}. Furthermore, the switching

$$U_{buck} - v_{dp} = L_{dp} \frac{\Delta I_{dp}}{t_2 - t_1}, \tag{27}$$

$$k_1 = \frac{U_{buck} - v_{dp}}{L_{dp}}, \tag{28}$$

Fig. 2 Working mode of the APF circuit: **a** MMC transfers energy to the APF circuit; **b** APF circuit transfers energy to the MMC

$$v_{dp} = L_{dp} \frac{\Delta I_{dp}}{t_3 - t_2}, \tag{29}$$

$$T_{APF} = t_4 - t_1. \tag{30}$$

In one switching cycle, the energy releasing process of the inductor and capacitor from the APF circuit to the MMC is displayed in Fig. 2b. At $t = t_5$, S_3 turns off and S_4 turns on, the APF circuit works in the Boost state, and the capacitor C_{dp} begins to release energy to the inductor L_{dp}. At this time, the inductor current i_{dp} in the APF circuit increases linearly, and the mathematical relationship of the voltage v_{dp} and the current i_{dp} in the APF circuit is shown in (31), and the change rate of the inductor current k_2 is shown in (32). At $t = t_6$, the power switching device S_3 turns on and S_4 turns off, and the inductor and capacitor in the APF circuit begin to release energy to the MMC. When $t = t_7$, the energy is all transferred to the MMC. In addition, the capacitor current i_{dp} and the voltage v_{dp} have the mathematical relationship shown in (33). The switching period T_{APF} is obtained as (34):

$$v_{dp} = L_{dp} \frac{\Delta I_{dp}}{t_6 - t_5}, \tag{31}$$

$$k_2 = \frac{v_{dp}}{L_{dp}}, \tag{32}$$

$$U_{buck} - v_{dp} = L_{dp} \frac{\Delta I_{dp}}{t_7 - t_6}, \tag{33}$$

$$T_{APF} = t_8 - t_5. \tag{34}$$

According to energy conservation and the impulse area equivalent law, in one switching period, the following results can be obtained, respectively:

$$\begin{cases} \frac{1}{2} k_1 (t_2 - t_1)(t_3 - t_1) = \overline{i_{dp}} T_{APF} \\ \frac{1}{2} k_2 (t_6 - t_5)(t_7 - t_5) = \overline{i_{dp}} T_{APF} \end{cases}, \tag{35}$$

where i_{dp} is the average current in each switch period T_{APF}.

According to (35), the duty factor D_1 of the switching device S_3 when the MMC transfers energy to the APF circuit, and the duty factor D_2 of S_3 when the APF circuit transfers energy to the MMC can be obtained as (36):

$$\begin{cases} D_1 = \sqrt{\dfrac{2L_{dp} v_{dp} \overline{i_{dp}}}{U_{buck}(U_{buck} - v_{dp}) T_{APF}}} \\ D_2 = \sqrt{\dfrac{2L_{dp}(U_{buck} - v_{dp}) v_{dp} \overline{i_{dp}}}{U_{buck} v_{dp} T_{APF}}} \end{cases}. \tag{36}$$

Equation (36) dictates the duty factor of the switch device S_3 when there is energy interaction within the MMC and APF topology. According to the duty factor of the power device S_3 in the APF, the terminal voltage of the capacitor in the APF circuit can track the reference voltage shown in (24).

Fig. 3 Pictures of experimental platform
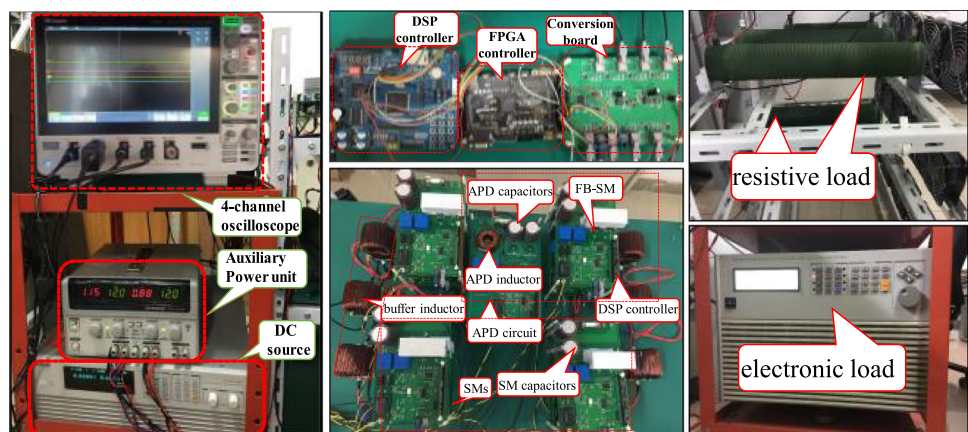
Table 1 Experimental and simulation parameters

Parameters	Simulation	Experiment
dc bus voltage (U_{dc})	10 kV	400 V
Number of SMs each arm ($2N$)	8	4
Rated SM capacitor voltage (U_{Cref})	1250 V	100 V
SM capacitance (C)	1.36 mF	1.36 mF
SM capacitance (C_{dp})	1.36 mF	1.36 mF
RL load	/	12.6 Ω/2 mH
Arm inductor (L)	9mH	9mH
APF inductance (L_{dp})	430 µH	430 µH
SM switching frequency (f)	2 kHz	2 kHz
APF switching frequency (f_{APF})	2 kHz	2 kHz
Fundamental frequency (f)	0–10 Hz	5 and 10 Hz
Voltage modulation index (k)	/	0.3
Rated rotor speed	750 r/min	/
Mechanical torque	20 N m	/

4 Simulations and experimental results

4.1 Experimental results

To verify that the capacitor voltage fluctuation suppression approach is applicable to the APF-MMC topology, experimental results obtained with the APF-MMC and the conventional MMC are compared on the single-phase experimental prototype platform depicted in Fig. 3. With reference to the experimental parameters outlined in [19] and [31], Table 1 showcases the comprehensive prototype platform parameters, while Figs. 4, 5, 6, 7, 8, 9, 10, 11, and 12 present the corresponding results.

4.1.1 Experimental comparison at $f = 10$ Hz

Figure 4a illustrates the SM capacitor oscillation voltage of the conventional MMC, with a peak value of approximately 20.3 V. For comparison, when the frequency of the infused components $f_h = 100$ Hz, the voltage ripple of the top sub-arm capacitor of the APF-MMC upper arm is 9.3 V, as displayed in Fig. 4b. In a similar fashion, Fig. 4c, d portrays the voltage

Fig. 4 Comparison of the SM capacitor voltage at $f = 10$ Hz: **a** traditional MMC; **b** top sub-arm SM of the upper arm in the APF-MMC topology; **c** bottom sub-arm SM of the upper arm in the APF-MMC topology; **d** bottom sub-arm SM of the lower arm in the APF-MMC topology

(a)

(b)

(c)

(d)
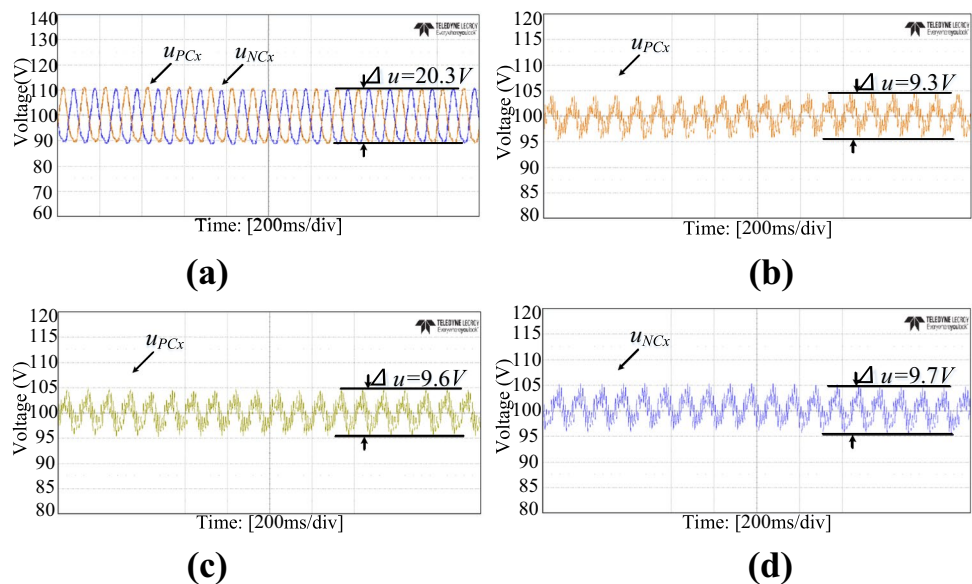
Fig. 5 Comparison of the upper and lower arm currents at $f = 10$ Hz: **a** traditional MMC topology; **b** APF-MMC topology

(a)

(b)
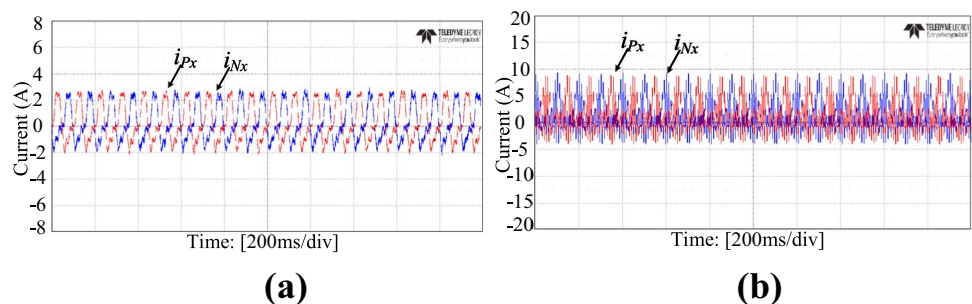
magnitudes of the lower sub-arm capacitors in the APF-MMC. These values measure 9.6 V and 9.7 V, respectively. When comparing Fig. 4a with Fig. 4b–d, it becomes evident that the voltage ripple observed in the capacitor of the APF-MMC is diminished to a mere 46.8% of the corresponding ripple in conventional MMC, which is achieved through the injection application of high-frequency voltage and current.

As displayed in Fig. 5a, the maximum of the arms current in the conventional MMC topology is about 3.3 A, which is constituted of the base frequency part (at this time, $f = 10$ Hz). The arms current of the APF-MMC is described in Fig. 7b, and the maximum amplitude is about 9.2 A. Comparing Fig. 5a with Fig. 5b, it is evident that the growth of arms current amplitude of the APF-MMC is a result of the injection of high-frequency current, which results in additional power dissipation and current stress of the power switch devices in the SM.

4.1.2 Experimental comparison at $f = 5$ Hz

In Fig. 6a, it is illustrated that the classical MMC capacitors experience a maximum voltage fluctuation of 33.2 V.

However, when high-frequency components with a frequency of $f_h = 100$ Hz are introduced, Fig. 6b showcases the voltage fluctuations of the top sub-arm capacitor in the upper arm of the APF-MMC, with a peak ripple value of approximately 11.9 V. Similarly, Fig. 6c, d reveals the capacitor voltage of the top sub-arm in the Mid-arm and the bottom sub-arm in the lower arms of the APF-MMC, with ripple amplitudes of 12.1 V. Combining Fig. 6a–d, it can be seen that as a result of the injected components, the capacitor voltage fluctuation of the APF-MMC circuit is decreased to 36.14% of that of the traditional MMC. When compared to the base frequency of $f = 10$ Hz, it is observed that the APF-MMC topology with a base frequency of 5 Hz exhibits a higher rate of change in the SM voltage ripple. This observation further validates the validity of the APF-MMC in suppressing the voltage ripple of SM capacitors during low-frequency operation.

In Fig. 7a, the arm current of the classical MMC is depicted. These currents comprise the base frequency component, operating at a frequency of 5 Hz, with a maximum amplitude reaching approximately 2.88 A. Figure 7b displays arm currents of the improved topology, of which the

Fig. 6 Comparison of the SM capacitor voltage at $f = 5$ Hz: **a** traditional MMC; **b** top sub-arm SM of the upper arm in the APF-MMC topology; **c** bottom sub-arm SM of the upper arm in the APF-MMC topology; **d** bottom sub-arm SM of the lower arm in the APF-MMC topology
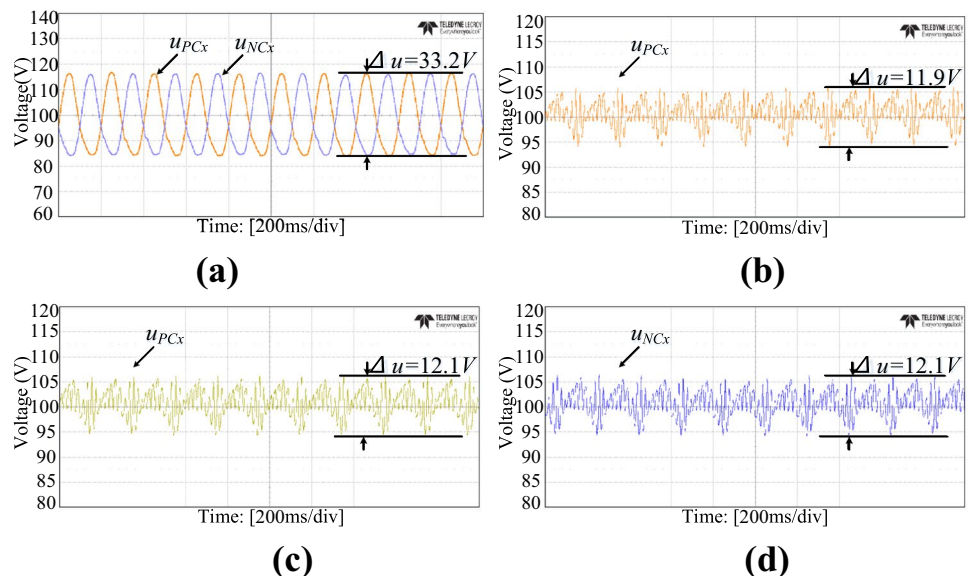
Fig. 7 Comparison of the upper and lower arm currents at $f = 5$ Hz: **a** traditional MMC topology; **b** APF-MMC topology
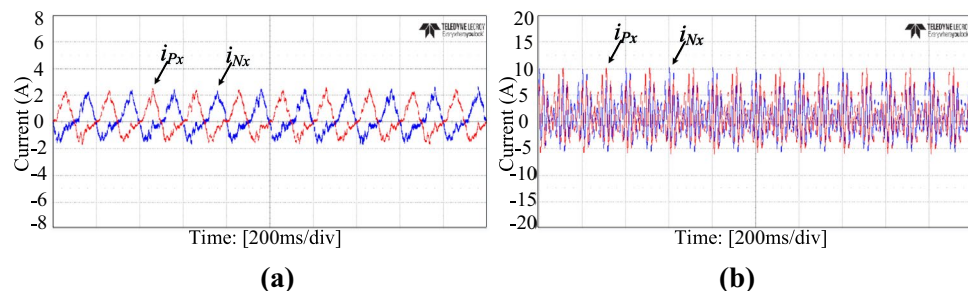
amplitude is about 10.1 A. When comparing Fig. 7a with Fig. 7b, it becomes evident that as a result of the injected current, the maximum value of the arm current for the APF-MMC experiences a significant increase, resulting in increases of the power dissipation and current stress in the SM power switch parts. Given the brief ramp-up time of the motor, the additional power dissipation from the synchronous machine remains minimal throughout the entire operating cycle. Therefore, the impact of the elevated arm currents on the system can be disregarded. The amplitude of arm currents can be diminished by optimizing the high-frequency components in practical applications.

4.1.3 Output voltage and current of the APF-MMC

To ascertain the elimination of the impact of the high-frequency voltage on the external characteristics of the MMC topology, an additional APF circuit is utilized as a hardware degree of freedom. The experimental findings, depicted in Fig. 8a, b, present the external characteristics at fundamental frequencies of 5 Hz and 10 Hz, respectively. Concurrently, Fig. 9a, b showcases the respective output voltage waveforms of the APF. Notably, it can be observed that high-frequency harmonics with significant amplitudes are absent, underscoring the successful mitigation of the injected component influence on the external characteristics of the topology.

Based on the aforementioned experimental findings, it can be concluded that the APF-MMC topology, in comparison to the conventional MMC topology, exhibits a noteworthy reduction in voltage ripples across the SM capacitors.

Furthermore, the injected high-frequency voltage does not influence the external output characteristics of the APF-MMC topology.

4.2 Motor drive simulation results

A simulation of a PMSM is conducted using PLECS software, since the availability of an experimental motor drive is limited. The PMSM is regulated by both an inner vector control loop and an outer speed control loop, and the d-axis current i_d is set to 0. Notably, the voltage level applied in motor drive applications typically does not surpass 10 kV. The motor parameter is outlined in Table 1.

Simulation waveforms for the conventional MMC from standstill (0 Hz) to 150 r/min (10 Hz) are shown in Fig. 10. It can be obtained from Fig. 10 that the traditional MMC topology has a large capacitor voltage ripple with low-frequency operation, which requires a large capacitor value to suppress the voltage ripple, which limits its application. In contrast, the APF-MMC simulation results with the introduced operation approach are displayed in Fig. 11.

Obviously, the SM capacitor voltage fluctuation amplitude is considerably suppressed. It can be obtained from Figs. 10 and 11 that the lower the working frequency, the better the suppression of the SM voltage fluctuation. In addition, by controlling the additional APF topology, the impact caused by the infused high-frequency voltage to the output characteristics of the MMC topology can be removed. Furthermore, due to the short start-up time of the
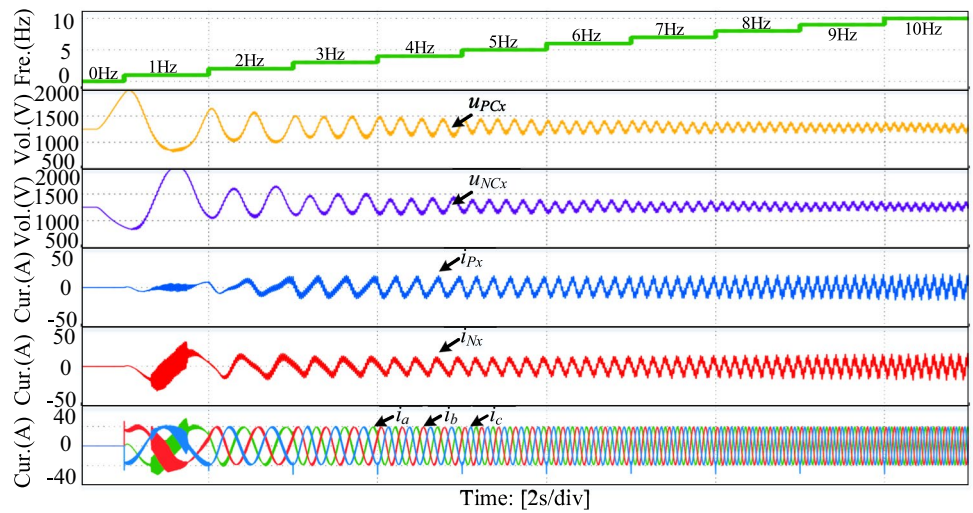
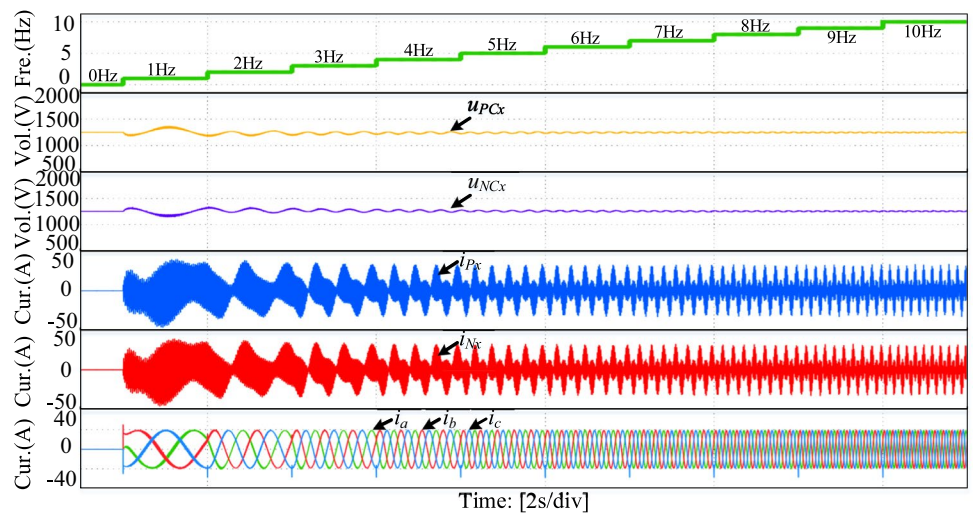Fig. 8 Output wave of the APF-MMC: **a** $f = 10$ Hz; **b** $f = 5$ Hz

(a)　　(b)
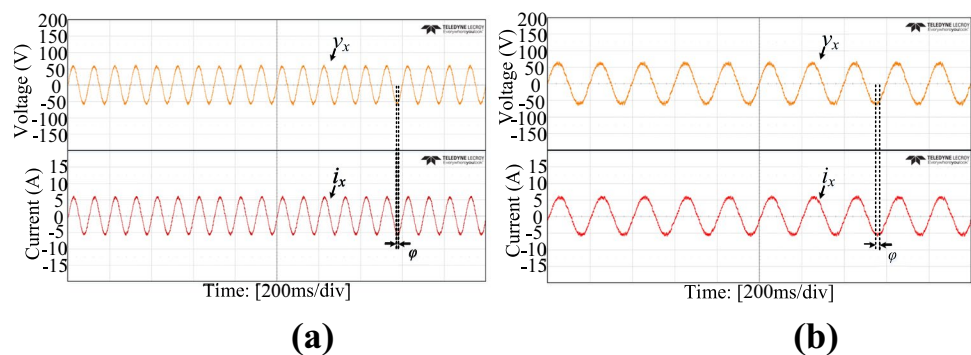
Fig. 9 Output voltage of the APF circuit: **a** $f = 10$ Hz; **b** $f = 5$ Hz
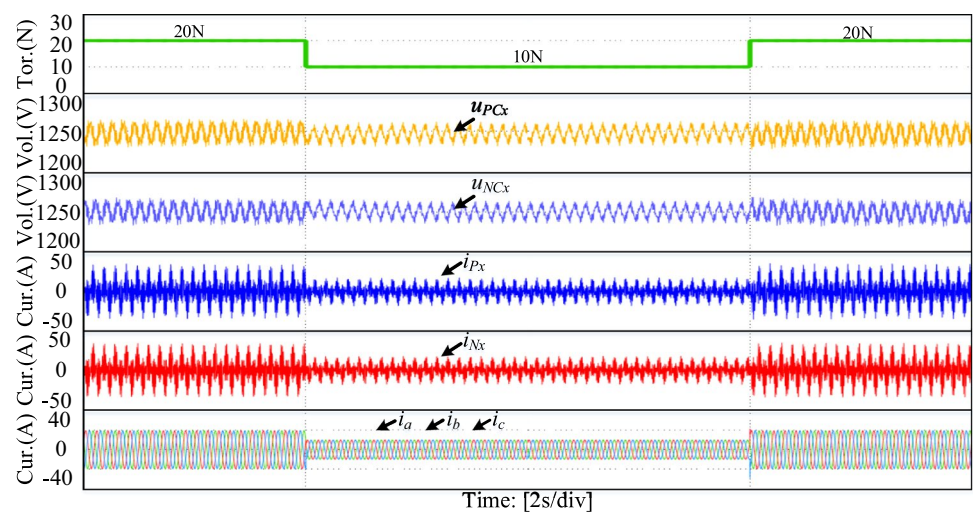

(a)　　(b)
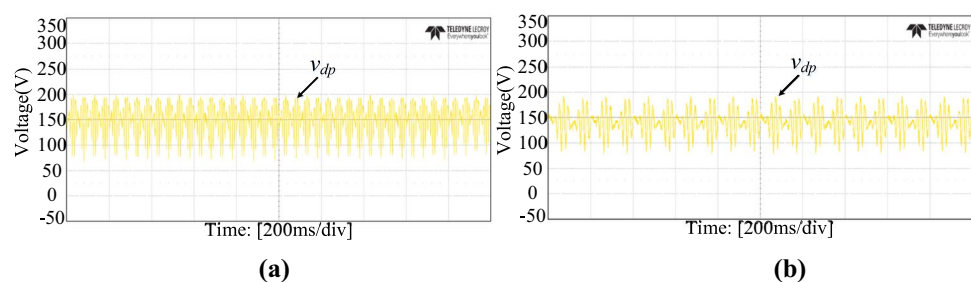
Fig. 10 Simulated run-up wave-forms of a PMSM driven by the traditional MMC

Fig. 11 Simulated run-up wave-forms of a PMSM driven by the APF-MMC

Fig. 12 Simulated waveforms of the APF-MMC when the load changes

motor, the power losses caused by the large arm current can be ignored.

To verify the transient characteristics of the APF-MMC topology with the introduced control approach, the mechanical torque of the motor is reduced from the rated torque to a light torque and then back to the rated torque. The corresponding simulation outcomes are given in Fig. 12. There is no marked over-shoot at the moment of torque switching, and the APF-MMC with the introduced control method can achieve a new stable state in a few basic cycles. In addition, it has been confirmed that the introduced APF-MMC topology with the suggested regulation approach can effectively drive the motor under low-frequency operation.

5 Conclusion

This study presented an APF-MMC topology for low-frequency operation. It accomplished suppression of SM capacitor voltage ripples by incorporating two adjustable degrees of freedom for the injected high-frequency voltage and current. Additionally, the hardware degrees of freedom within the APF circuit were shown to effectively mitigate the influence of the injected high-frequency voltage on the output characteristics of the topology.

The composition and analogous representation of the APF-MMC circuit were meticulously expounded upon and minutely scrutinized. Subsequently, a control technique was proposed for the APF branch, ensuring the seamless operation of this topology. Finally, prototypes of both the APF-MMC and the conventional MMC were constructed and subjected to meticulous comparative experimentation. Furthermore, the utilization of the three-phase APF-MC for motor drive applications was assessed via a comprehensive simulation platform. Upon direct comparison with the traditional MMC, the APF-MMC circuit was shown to exhibit commendable performance, particularly in low-frequency scenarios, as substantiated by meticulous simulation and exhaustive experimental evaluations.

Data availability The authors confirm that the data supporting the findings of this study are available within the article.

References

1. Zhou, L., Chen, C., Xiong, J., Zhang, K.: A robust capacitor voltage balancing method for CPS-PWM-based modular multilevel converters accommodating wide power range. IEEE Trans. Power Electron. **37**(12), 14306–14316 (2022)
2. Tang, S., Chen, M., Jia, G., Zhang, C.: Topology of current-limiting and energy-transferring DC circuit breaker for DC distribution networks. CSEE J. Power Energy Syst. **6**(2), 298–306 (2020)
3. Poblete, P., Pizarro, G., Droguett, G., Núñez, F., Judge, D., et al.: Distributed neural network observer for submodule capacitor voltage estimation in modular multilevel converters. IEEE Trans. Power Electron. **37**(9), 10306–10318 (2022)
4. Li, B., Zhang, Y., Wang, G., Sun, W., Xu, D., et al.: A modified modular multilevel converter with reduced capacitor voltage fluctuation. IEEE Trans. Ind. Electron. **62**(10), 6108–6119 (2015)
5. Jia, G., Chen, M., Tang, S., Zhang, C., Zhu, G.: Active power decoupling for a modified modular multilevel converter to decrease submodule capacitor voltage ripples and power losses. IEEE Trans. Power Electron. **36**(3), 2835–2851 (2021)
6. Kong, Z., Huang, X., Wang, Z., Xiong, J., Zhang, K.: Active power decoupling for submodules of a modular multilevel converter. IEEE Trans. Power Electron. **33**(1), 125–136 (2018)
7. Ilves, K., Norrga, S., Harnefors, L., Nee, H.-P.: On energy storage requirements in modular multilevel converters. IEEE Trans. Power Electron. **29**(1), 77–88 (2014)
8. Lesnicar, A., Marquardt, R.: An innovative modular multilevel converter topology suitable for a wide power range. In: Proceedings of IEEE Power Tech Conference, June 23–26, 2003, vol. 3, Bologna, Italy, p. 6 (2003)
9. Picas, R., Pou, J., Ceballos, S., Agelidis, V.G., Saeedifard, M.: Minimization of the capacitor voltage fluctuations of a modular multilevel converter by circulating current control. In: Proceedings of IEEE IECON, Montreal, QC, Canada, October 25–28, 2012, pp. 4985–4991 (2012)
10. Pou, J., Ceballos, S., Konstantinou, G., Agelidis, V.G., Picas, R., et al.: Circulating current injection methods based on instantaneous information for the modular multilevel converter. IEEE Trans. Ind. Electron. **62**(2), 777–788 (2015)
11. Engel, S.P., De Doncker, R.W.: Control of the modular multilevel converter for minimized cell capacitance. In: Proceedings of EPE, Birmingham, U.K., 30 August–1 September 2011, pp. 1–10
12. Picas, R., Pou, J., Ceballos, S., Zaragoza, J., Konstantinou, G., et al.: Optimal injection of harmonics in circulating currents of modular multilevel converters for capacitor voltage ripple minimization. In: Proceedings of IEEE ECCE Asia, 2013, pp. 318–324
13. Li, B., Zhou, S., Xu, D., Yang, R., Cecati, C.: An improved circulating current injection method for modular multilevel converters in variable-speed drives. IEEE Trans. Ind. Electron. **63**(11), 1 (2016)
14. Korn, A.J., Winkelnkemper, M., Steimer, P.: Low output frequency operation of the modular multilevel converter. In: Proceedings of IEEE ECCE, 2010, pp. 3993–3997 (2010)
15. Hagiwara, M., Hasegawa, I., Akagi, H.: Start-up and low-speed operation of an electric motor driven by a modular multilevel cascade inverter. IEEE Trans. Ind. Appl. **49**(4), 1556–1565 (2013)
16. Jung, J., Lee, H., Sul, S.-K.: Control strategy for improved dynamic performance of variable-speed drives with modular multilevel converter. IEEE J. Emerg. Sel. Top. Power Electron. **3**(2), 371–380 (2015)
17. Debnath, S., Qin, J., Saeedifard, M.: Control and stability analysis of modular multilevel converter under low-frequency operation. IEEE Trans. Ind. Electron. **62**(9), 5329–5339 (2015)
18. Li, A., Lin, L., Xu, C., Yang, S.: Coordinated optimization of capacitor voltage ripple and current stress minimization for modular multilevel converter. In: 2018 IEEE International Power Electronics and Application Conference and Exposition, Shenzhen, 2018, pp. 1–6 (2018)

19. Huang, M., Zou, J., Ma, X., Li, Y., Han, M.: Modified modular multilevel converter to reduce submodule capacitor voltage ripples without common-mode voltage injected. IEEE Trans. Ind. Electron. **66**(3), 2236–2246 (2019)

20. Chen, R., Liu, Y., Peng, F.Z.: DC capacitor-less inverter for single phase power conversion with minimum voltage and current stress. IEEE Trans. Power Electron. **30**(10), 5499–5507 (2015)

21. Liang, S., Lu, X., Chen, R., Liu, Y., Zhang, S., et al.: A solid state variable capacitor with minimum DC capacitance. In: 2014 IEEE Applied Power Electronics Conference and Exposition—APEC 2014, Fort Worth, TX, 2014, pp. 3496–3501 (2014)

22. Tsuno, K., Shimizu, T., Wada, K., Ishii, K.: Optimization of the DC ripple energy compensating circuit on a single-phase voltage source PWM rectifier. In: 2004 IEEE 35th Annual Power Electronics Specialists Conference (IEEE Cat. No.04CH37551), Aachen, Germany, 2004, pp. 316–321 (2004)

23. Mazumder, S.K., Burra, R.K., Acharya, K.: A ripple-mitigating and energy-efficient fuel cell power-conditioning system. IEEE Trans. Power Electron. **22**(4), 1437–1452 (2007)

24. Cao, X., Zhong, Q., Ming, W.: Ripple eliminator to smooth DC-Bus voltage and reduce the total capacitance required. IEEE Trans. Power Electron. **62**(4), 2224–2235 (2015)

25. Harb, S., Mirjafari, M., Balog, R.S.: Ripple-port module-integrated inverter for grid-connected PV applications. IEEE Trans. Ind. Appl. **49**(6), 2692–2698 (2013)

26. Jia, G., Chen, M., Tang, S., Zhang, C., Zhao, B.: A modular multilevel converter with active power filter for submodule capacitor voltage ripples and power losses reduction. IEEE Trans. Power Electron. **35**(11), 11401–11417 (2020)

27. Sun, Y., Liu, Y., Su, M., Xiong, W., Yang, J.: Review of active power decoupling topologies in single-phase systems. IEEE Trans. Power Electron. **31**(7), 4778–4794 (2016)

28. Zhou, Y., Jiang, D., Guo, J., Hu, P., Liang, Y.: Analysis and control of modular multilevel converters under unbalanced conditions. IEEE Trans. Power Deliv. **28**(4), 1986–1995 (2013)

29. Song, S., Liu, J., Ouyang, S., Chen, X.: An improved high-frequency common-mode voltage injection method in modular multilevel converter in motor drive application. In: 2018 IEEE Applied Power Electronics Conference and Exposition (APEC), San Antonio, TX, 2018, pp. 2496–2500 (2018)

30. Ming, H., Jianlong, Z., Xikui, M., Yang, L., Mingyue, H.: Modified modular multilevel converter to reduce sub-module capacitor voltage ripples without common-mode voltage injected. IEEE Trans. Ind. Electron. **66**(3), 2236–2246 (2019)

31. Wang, K., Li, Y., Zheng, Z., Xu, L.: Voltage balancing and fluctuation suppression method of floating capacitors in a new modular multilevel converter. IEEE Trans. Ind. Electron. **60**(5), 1943–1954 (2013)

32. Wang, R., Wang, F., Boroyevich, D., Burgos, R., Lai, R., et al.: A high power density single-phase PWM rectifier with active ripple energy storage. IEEE Trans. Power Electron. **26**(5), 1430–1443 (2011)

Guanlong Jia was born in Henan, China. He received his Ph.D. degree from Zhejiang University, Hangzhou, China, in 2021. Since June 2021, he has been with the Hebei University of Technology, Tianjin, China, where he is presently working as a lecturer. His current research interests include circuit breakers, multilevel converters, high-power electronics, control algorithms, and pulse-width modulation techniques.
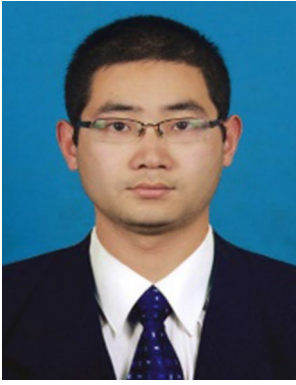

Mingshuo Li was born in Hebei, China. He is presently working toward his M.S. degree in Electrical Engineering at the Hebei University of Technology, Tianjin, China. His current research interests include modular multilevel converters, DC circuit breakers, and HVDC fault protection techniques.

Lin Chen was born in Hebei, China. He is presently working toward his B.S. degree in Electrical Engineering at the Hebei University of Technology, Tianjin, China. His current research interests include modular multilevel converters, DC circuit breakers, and HVDC fault protection techniques.


Binhao Shi was born in Hebei, China. He is presently working toward his M.S. degree in Electrical Engineering at the Hebei University of Technology, Tianjin, China. His current research interests include modular multilevel converters, DC circuit breakers, and HVDC fault protection techniques.

Feng Niu was born in Hebei, China, in 1986. He received his B.S. and Ph.D. degrees from the Hebei University of Technology, Tianjin, China, in 2009 and 2015, respectively. From 2016 to 2018, he was a postdoctoral research fellow in the College of Electrical Engineering, Zhejiang University, Hangzhou, China. He is presently working as a professor in the School of Electrical Engineering, Hebei University of Technology. His current research interests include motor systems and control, and intelligent electrical equipment.
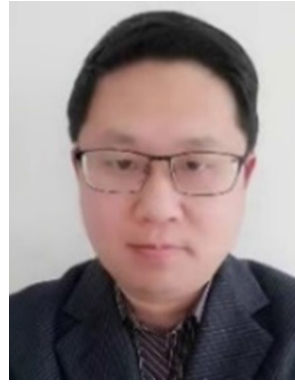
Yu Tang received his B.S. and Ph.D. degrees from the Nanjing University of Aeronautics and Astronautics (NUAA), Nanjing, China, in 2003 and 2008, respectively. Since 2018, he has been with the State Key Laboratory of Reliability and Intelligence of Electrical Equipment, Hebei University of Technology, Tianjin, China. His current research interests include the application of power electronics in renewable energy generation. Dr. Tang is a guest associate editor of the *IEEE TRANSACTIONS ON POWER ELECTRONICS*.